nanomaterials

MDPI

Article

W_2C/WS_2 Alloy Nanoflowers as Anode Materials for Lithium-Ion Storage

Thang Phan Nguyen and Il Tae Kim *

Department of Chemical and Biological Engineering, Gachon University, Seongnam-si, Gyeonggi-do 13120, Korea; phanthang87@gmail.com

* Correspondence: itkim@gachon.ac.kr

Received: 20 June 2020; Accepted: 6 July 2020; Published: 9 July 2020

Abstract: Recently, composites of MXenes and two-dimensional transition metal dichalcogenides have emerged as promising materials for energy storage applications. In this study, W_2C/WS_2 alloy nanoflowers (NFs) were prepared by a facile hydrothermal method. The alloy NFs showed a particle size of 200 nm–1 µm, which could be controlled. The electrochemical performance of the as-prepared alloy NFs was investigated to evaluate their potential for application as lithium-ion battery (LIB) anodes. The incorporation of W_2C in the WS_2 NFs improved their electronic properties. Among them, the W_2C/WS_2_4h NF electrode showed the best electrochemical performance with an initial discharge capacity of 1040 mAh g^{-1} and excellent cyclability corresponding to a reversible capacity of 500 mAh g^{-1} after 100 cycles compared to that of the pure WS_2 NF electrode. Therefore, the incorporation of W_2C is a promising approach to improve the performance of LIB anode materials.

Keywords: W_2C; WS_2; hydrothermal; nanoflowers; lithium-ion batteries

1. Introduction

Two-dimensional (2D) materials such as graphene and transition metal chalcogenides show great potential for energy storage and conversion applications owing to their large surface area, high conductivity, and good physical and chemical stability [1–12]. Among these 2D materials, MXenes, which have been discovered recently, have been extensively investigated for energy storage applications. It should be noted that MXenes are the transition metal carbides/nitride, which have graphene-like structure, possessing many advantages of 2D materials such as high conductivity, flexibility, easy processing, and so on [13]. Mashtalir et al. synthesized intercalated Ti_3C_2 flakes with high stability and the charging rate for application as an anode material for lithium-ion batteries (LIBs) [14]. Naguib et al. prepared niobium and vanadium carbide LIB anodes with high rate capacity [15]. The MXene anodes exhibited excellent electrochemical performance at high currents because of their low diffusion barrier [16]. In addition, Fe_3O_4@Ti_2C_3 LIB anodes exhibited an ultrahigh capacity of approximately 747 mAh g^{-1} at 1 C for 1000 cycles. Moreover, these materials exhibited a capacity of approximately 278 mAh g^{-1} at the high rate of 5 C [17]. Zhang et al. have demonstrated the use of MXenes as conductive binders for viscous aqueous inks of silicon materials, which were used as high-capacity anode materials for LIBs [18]. In these materials, MXenes not only acted as a conductive network for Si particles, but also improved the mechanical stability of the material.

Tungsten metal compounds such as oxides, chalcogenides, and carbides are used in a wide range of applications such as catalysis, energy conversion, and energy storage [19–27]. Feng et al. prepared WS_2 nanoflakes with a high reversible capacity of 680 mAh g^{-1} for 20 cycles as anode materials for LIBs [27]. Srinivaas et al. have prepared highly rich 1T WS_2 phase in few layered nanoflowers (NFs) with stable electrochemical performance and a high initial capacity of approximately 890 mAh g^{-1} as anode materials for LIBs [28]. W_2C is a good catalyst. When grown on carbon nanotubes, it exhibits

high photo/electrocatalytic performance for the hydrogen evolution reaction [26,29]. Simulation results have shown that W_2C can exhibit an ultra-fast loading of lithium ions owing to its low diffusion barrier of about 0.045–0.13 eV [30]. Thus, the combination of WS_2 and W_2C is expected to yield a promising LIB anode material.

In this study, we prepared a W_2C/WS_2 NF composite via a facile hydrothermal process. By controlling the reaction time, alloy NFs with different sizes could be prepared. The structures, chemical compositions, and binding states of the as-prepared NFs were investigated. Finally, the potential of the W_2C/WS_2 NFs for LIB anode applications was investigated. The NFs showed promising electrochemical performance and excellent Li storage.

2. Materials and Methods

2.1. Chemical Materials

Tungsten (VI) chloride (WCl_6, 99.9% trace metals basis, Sigma-Aldrich Inc., St. Louis, MO, USA), thioacetamide (C_2H_5NS, 99%, Sigma-Aldrich, Sigma-Aldrich Inc., St. Louis, MO, USA), amorphous carbon black Super-P (C, approximately 40 nm 99.99%, Alfa Aesar Inc., MA, USA), absolute ethanol (C_2H_5OH, Alpha Aesar Inc., MA, USA), and polyvinylidene fluoride (PVDF, 534,000 M_W, Sigma-Aldrich, Sigma-Aldrich Inc., St. Louis, MO, USA) were used as received without any treatment.

2.2. Synthesis of W_2C/WS_2 NFs

The W_2C/WS_2 alloy NFs were prepared according to a previously reported procedure [31]. Briefly, 0.6 g of WCl_6 was dispersed as the W source in a 20 mL tube with 4 mL of absolute ethanol. For the sulfur and carbon source, 1.2 g of thioacetamide was dispersed in 4 mL of absolute ethanol under stirring. Then, the WCl_6 solution was quickly added to the thioacetamide solution, and the resulting solution was stirred for 5 min. Then, 30 mL of deionized (DI) water was added, and the solution was stirred for 1 h. Then, the reaction mixture was transferred to a 50 mL polypropylene-lined autoclave and heated in an oven at 250 °C for 2, 4, and 12 h to obtain the W_2C/WS_2_2h, W_2C/WS_2_4h, and W_2C/WS_2_12h precipitates, respectively. These precipitates were washed four times with ethanol and DI water and were then dried in an oven at 60 °C to obtain the W_2C/WS_2 powders.

2.3. Characterization

X-ray diffraction (XRD) (D/MAX-2200 Rigaku, Tokyo, Japan) was used to analyze the structure of the samples. The XRD patterns of the samples were recorded over the 2θ range of 5–70°. The morphologies, structures, and sizes of the samples were investigated by scanning electron microscopy (SEM) (Hitachi S4700, Tokyo, Japan) and transmission electron microscopy (TEM) (TECNAI G2F30, FEI corp., OR, USA). The Raman spectra of the samples were acquired using a Raman spectrometer (Lab RAM HR, Horiba JobinYvon, Horiba Ltd., Kyoto, Japan, 532 nm laser excitation). X-ray photoelectron spectroscopy (XPS) (Axis Ultra DLD, Kratos Analytical Ltd, Kyoto, Japan) under a high vacuum of 1.6×10^{-10} mbar with a monochromatic Al Kα line was used to investigate the chemical compositions and atomic binding of the samples.

2.4. Electrochemical Measurements

The LIBs were assembled using coin-type cells (CR 2032, Rotech Inc., Gwangju, Korea). The working electrode was prepared by casting a slurry of 70% active material (W_2C/WS_2 alloy NFs), 15% conductive carbon black (Super-P), and 15% PVDF in N-methyl-2-pyrrolidinone on a copper foil by doctor blading. After drying in a vacuum oven at 70 °C for 12 h, the electrodes were punched into circular discs with a diameter of 12 mm. The battery half-cell structures were assembled under an Ar_2 atmosphere in a glovebox. A lithium foil, polyethylene, and 1M $LiPF_6$ in ethylene carbonate/diethylene carbonate (1:1 in volume) were employed as the reference electrode, separator, and electrolyte, respectively. Galvanostatic electrochemical charge–discharge measurements were

carried out using a battery cycle tester (WBCS3000, WonAtech, Seocho-gu, Seoul) over the voltage range of 0.1–3.0 V versus Li/Li^+. Cyclic voltammetry (CV) tests were carried out using ZIVE MP1 (WonAtech, Seocho-gu, Seoul) over the voltage range of 0.1–3.0 V at a scanning rate of 0.1 mV s^{-1}. Electrochemical impedance spectroscopic (EIS) measurements were carried out using a ZIVE MP1 (WonAtech, Seocho-gu, Seoul) over the frequency range of 100 kHz–0.1 Hz.

3. Results

For the synthesis of the W_2C/WS_2 NFs, the WCl_6 precursor was pre-mixed with absolute ethanol ($WCl_6 + xC_2H_5OH \rightarrow WCl_{6-x}(OC_2H_5)_x + xHCl$) before mixing with thioacetamide to prevent its unexpected reaction with moisture ($WCl_6 + xH_2O \rightarrow WCl_{6-x}(OH)_x + xHCl$) [31,32]. The hydrolysis of thioacetamide produced hydrosulfide, acetic acid, and ammonia ($2C_3H_5NS + 6H_2O \rightarrow 2H_2S + 3CH_3COOH + 2NH_3$). The introduction of hydrosulfide, acetic acid, and ethanol, respectively, acted as the sulfur and carbon sources for the formation of the W_2C/WS_2 alloys. Figure 1a–c show the SEM images of the W_2C/WS_2_2h, W_2C/WS_2_4h, and W_2C/WS_2_12h NFs, respectively. The particle sizes of the W_2C/WS_2_2h, W_2C/WS_2_4h, and W_2C/WS_2_12h NFs were 200, 400, and 1000 nm, respectively. The NFs showed a highly uniform structure, indicating that the synthesis procedure was highly reproducible. Each NF consisted of several leaves of W_2C nanosheets and WS_2 nanocrystals. Meanwhile, the WS_2 NFs synthesized without ethanol showed a complex structure because of the non-uniform dispersion of W (Figure 1d).

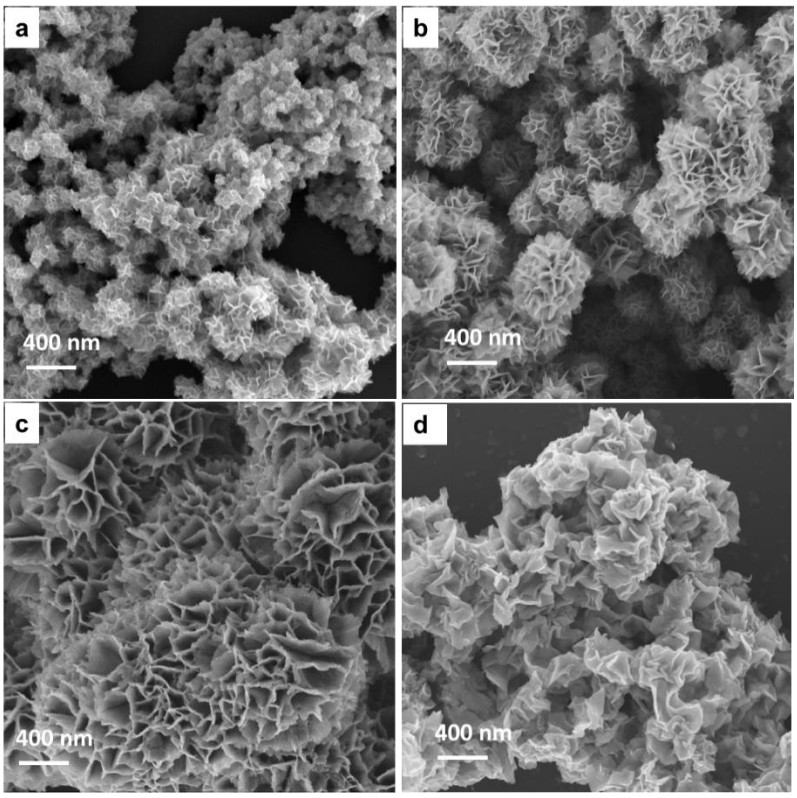

Figure 1. SEM images of the (**a**) W_2C/WS_2_2h, (**b**) W_2C/WS_2_4h, (**c**) W_2C/WS_2_12h, and (**d**) WS_2 NFs.

To further examine the structure of the W_2C/WS_2 NFs, powder XRD measurements were carried out over the 2θ range of 5–70° (Figure 2a). The XRD peaks of all the samples could be indexed to the hexagonal structure of W_2C and WS_2 [32–35]. It should be noted that the W_2C/WS_2_2h sample showed weak WS_2 peaks. Moreover, this sample showed broad W_2C peaks, indicating the small crystallite size of W_2C. The W_2C/WS_2_4h and W_2C/WS_2_12h samples showed clear W_2C and WS_2 peaks, indicating the co-existence of these hexagonal-structured materials. For comparison, a WS_2

sample was prepared using the same procedure as that used for preparing the W_2C/WS_2 NFs but without the addition of ethanol. This sample showed peaks corresponding to WS_2 only. Therefore, the addition of ethanol during the synthesis not only prevented the oxidation of WCl_6 but also contributed to the formation of carbide from the thioacetamide source. The structures of W_2C and WS_2 in the alloy NFs were examined by Raman spectroscopy (Figure 2b). The samples for Raman spectroscopy measurements were prepared on SiO_2/Si substrates, and a 532-nm wavelength laser source was used. The samples showed two peaks at 351.5 and 415.2 cm^{-1} corresponding to the in-plane mode vibration $E^1{}_{2g}$ and out-plane mode vibration A_{1g} of WS_2, respectively [2,36]. Moreover, the peaks detected at 700 and 805 cm^{-1} can be attributed to the stretching modes of W−C [26,37]. The D- and G-bands corresponding to the sp^3 and sp^2 carbon atoms in W_2C were observed at 1200–1700 cm^{-1}. These results indicate the co-existence of W_2C and WS_2 in the alloy NFs.

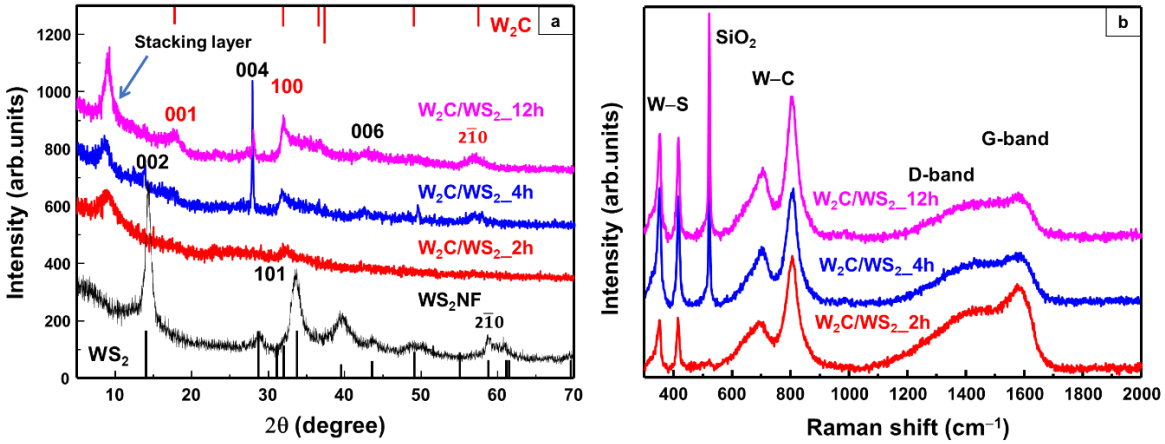

Figure 2. (**a**) X-ray diffraction (XRD) patterns and (**b**) Raman spectra of the W_2C/WS_2 alloy nanoflowers (NFs) synthesized by heating at 250 °C for 2, 4, and 12 h.

The structure of the W_2C/WS_2 alloy NFs was further examined using TEM. As can be observed from Figure 3a, the samples showed a uniform NF structure with many leaves. Some Moiré patterns with a size of about 0.9–1.0 nm could be observed in the TEM images of the samples (Figure 3b). This can be attributed to the formation of the W_2C/WS_2 interlayer spacing [31]. The lattice spacings of W_2C and WS_2 in the samples were also measured from their high-resolution TEM (HRTEM) image shown in Figure 3c. The distance spacings of the WS_2 (100) and W_2C (101) planes were measured to be 0.27 and 0.23 nm, respectively. These spacings are characteristic of these materials. Moreover, the selected-area electron diffraction (SAED) pattern shown in Figure 3d indicates that W_2C/WS_2 alloy NFs with a highly crystalline hexagonal structure were successfully fabricated.

The chemical compositions and atomic binding energies of the W_2C/WS_2 alloys were analyzed by XPS (Figure 4a–d). The survey scan XPS profiles of the alloys showed clear and sharp peaks corresponding to W, S, O, C, and Si (from substrate) (Figure 4a). No impurity peak was detected, indicating the high purity of the W_2C/WS_2 alloys. The high-resolution W 4f, S 2p, and C 1s spectra of the alloys are shown in Figure 4b–d, respectively. The W 4f peak consisted of doublet peaks corresponding to the W−C, W−S, and W−O bonds. The contribution of W−O bonding can be attributed to the slight oxidation on the surface of the alloys, which always occurs during the preparation or natural oxidation of a material in air [29]. The W 4f7/2 and W 4f5/2 peaks of the W−C doublet were observed at 31.9 and 34.1 eV, respectively, while those of the W−S doublet were observed at 32.4 and 34.6 eV, respectively. The W 4f7/2 and W 4f5/2 peaks of the W−O doublet were observed at 36.0 and 38.2 eV, respectively. The S 2p peak of the samples could be deconvoluted into the S 2p3/2 and S 2p1/2 peaks, which were observed at 161.4 and 162.6 eV, respectively. Furthermore, the slight oxidation of the surface of the alloys during the preparation resulted in the appearance of the S−O bond peak at about 169 eV. Finally, the C 1s peak of the samples could be deconvoluted into those corresponding to C−W bonding at

284.7 eV, C−O bonding at 286.2 eV, and C−OH bonding at 288.5 eV. This is consistent with the binding energy of C in carbide compounds [38].

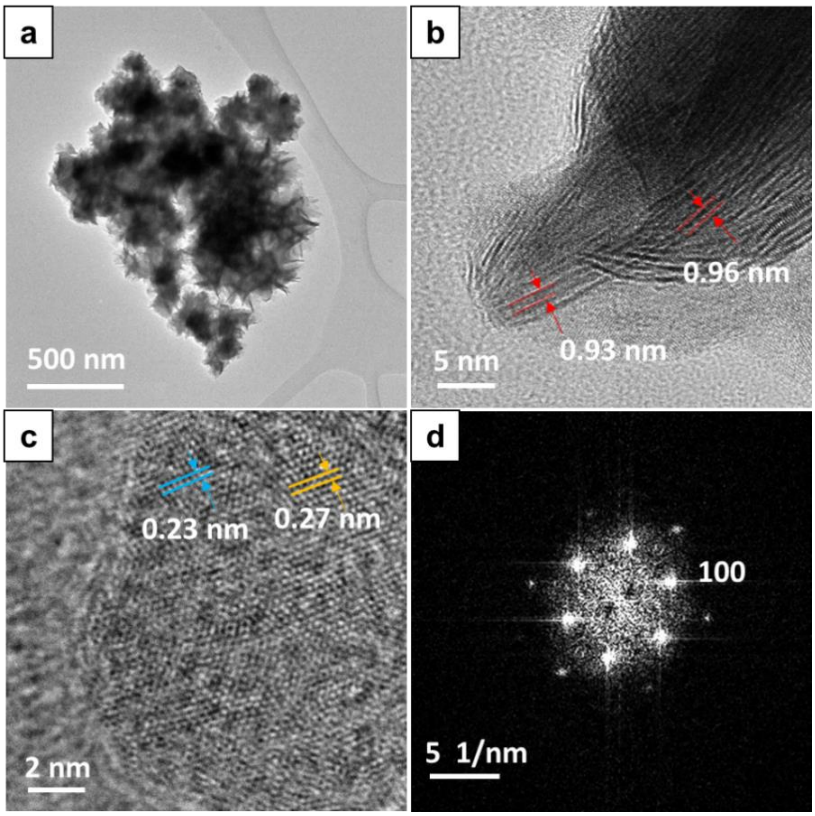

Figure 3. (**a**) TEM image; (**b**,**c**) HRTEM image and (**d**) selected-area electron diffraction (SAED) pattern of the W_2C/WS_2_4h NF sample.

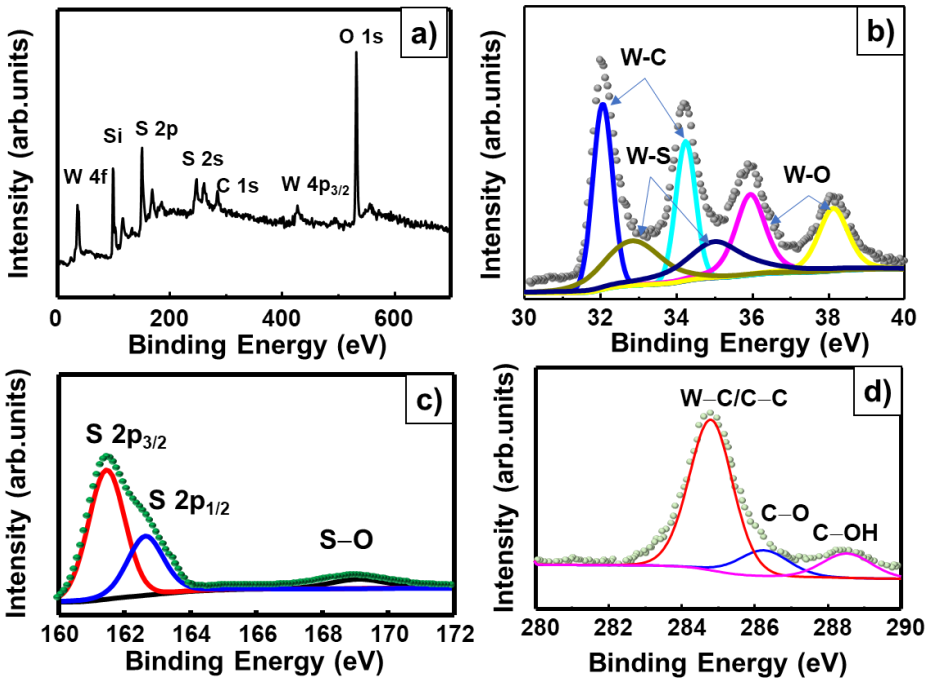

Figure 4. XPS profiles of the W_2C/WS_2 _4h NF sample with (**a**) survey scan spectrum and high-resolution (**b**) W 4f, (**c**) S 2p, and (**d**) C 1s spectra.

To evaluate the electrochemical performance of the alloys for application as LIB anode materials, their CV tests were carried out for three cycles over the voltage range of 0.1–3.0 V (Figure 5a–d). In the first cycle, the as-prepared WS_2NFs showed lithiation at 0.5, 1.2, and 1.4 V attributing to the reduction of WS_2 to Li_2S through multiple steps, including the formation of Li_xWS_2 and Li_2S [28]. The peak observed at 0.5 V corresponds to the conversion reaction ($4Li^+ + WS_2 + 4e^- \rightarrow 2Li_2S + W$) as well as the decomposition of the non-aqueous electrolyte to form the solid electrolyte interface (SEI) layer [28,39]. In the second cycle, the peak at 0.5 V disappeared because of the formation of the SEI and gel-like polymeric layers by the dissolution of Li_2S into the electrolyte, leading to its degradation [40]. The peaks at 1.2 and 1.4 V shifted to 1.27 V. An additional peak was observed at 1.9 V, indicating the insertion of Li into Li_xWS_2 [28]. Figure 5b–d show the cyclic voltammograms of the W_2C/WS_2_2h, W_2C/WS_2_4h, and W_2C/WS_2_12h samples, respectively. In the first cycle, the W_2C/WS_2_2h sample showed a small peak at about 1.1 V. In the second and third cycles, the sample showed reduction peaks at 1.25 and 1.9 V attributing to the multi-step lithiation of WS_2. Interestingly, the W_2C/WS_2_4h and W_2C/WS_2_12h samples with large NFs showed only a broad peak at 1.3–1.5 V in the first discharge cycle. This phenomenon can be attributed to the change in the work function of WS_2 by the addition of W_2C [31]. The changes in the work function of the alloys corresponded to the changes in their reduction potentials. The work function of the W_2C/WS_2 NFs increased from 4.31 to 4.7 eV with an increase in the reaction time from 2 to 12 h. The work function of the pure WS_2 sample was 4.95 eV. The bare WS_2 electrode showed lithiation peaks at 1.4 and 1.9 V. On the other hand, the W_2C/WS_2_2h and W_2C/WS_2_4h electrodes showed lithiation peaks at lower potentials at around 1.2–1.5 V. These samples did not show any lithiation peak at 1.9 V. Hence, it can be stated that the decrease in the work function resulted in a decrease in the lithiation potential of the samples. As shown by the XRD patterns, the W_2C/WS_2_2h sample showed broader W_2C peaks than the other samples, indicating that the W_2C crystallite size of this sample was smaller than those of the other samples. Therefore, the change in the second lithiation potential of the W_2C/WS_2_2h electrode was comparable to the initial potential of the WS_2 electrode because of the instability of its smaller W_2C crystals. The W_2C/WS_2_4h and W_2C/WS_2_12h electrodes only showed reduction peaks at about 1.2–1.5 V. This indicates that with an increase in the reaction time, the bonding between W_2C and WS_2 became stronger. The W_2C/WS_2 and WS_2 NFs showed similar oxidation peaks because of the restoration of the WS_2 structure at about 1.7–1.9 V and the oxidation of Li_2S ($Li_2S \rightarrow 2Li+S$) at about 2.3–2.5 V [39]. The W_2C/WS_2 NFs showed an oxidation peak at approximately 1.2 V, which was attributed to the delithiation of W_2C.

The initial discharge and charge voltage profiles of the W_2C/WS_2 and WS_2 NFs were obtained over the voltage range of 0.1–3.0 V at a scan rate of 100 mA g^{-1}, as shown in Figure 6a. The WS_2 NFs showed the charge and discharge capacities of 504.0 and 656.6 mAh g^{-1}, respectively. The W_2C/WS_2_2h, W_2C/WS_2_4h, and W_2C/WS_2_12h NFs showed the charge and discharge capacities of 595.2 and 935.2 mAh g^{-1}, 751.8 and 1040.5 mAh g^{-1}, 717.7 and 953.5 mAh g^{-1}, respectively. It has been reported that carbide materials are promising candidates for energy storage applications [41]. In this study, the addition of W_2C to the WS_2 NF sample improved its storage capacity. The cyclic performances of the W_2C/WS_2 and WS_2 NFs were evaluated over 100 cycles, as shown in Figure 6b. The alloys NF electrodes exhibited different electrochemical properties depending on the reaction time. For instance, after 10 cycles, the capacities of the W_2C/WS_2_2h and W_2C/WS_2_12h electrodes decayed rapidly by about 55%. After 30–40 cycles, the samples showed low stable capacities of 100–200 mAh g^{-1} with a high Coulombic efficiency of approximately 95–99%. On the other hand, the W_2C/WS_2_4h electrode showed excellent cyclic stability with a high capacity of 500 mAh g^{-1} after 100 cycles as compared to the other electrodes. The reasons why the W_2C/WS_2_4h electrode demonstrated the best performance are the stable binding of W_2C to WS_2 and the lowering of reduction potential in addition to the low resistance (discussed later). This sample showed a Coulombic efficiency of 97–98%. Meanwhile, the WS_2 NFs showed a Coulombic efficiency of 93–94% and a continuous decrease in the cyclic capacity to approximately 145 mAh g^{-1} during the 100th cycle.

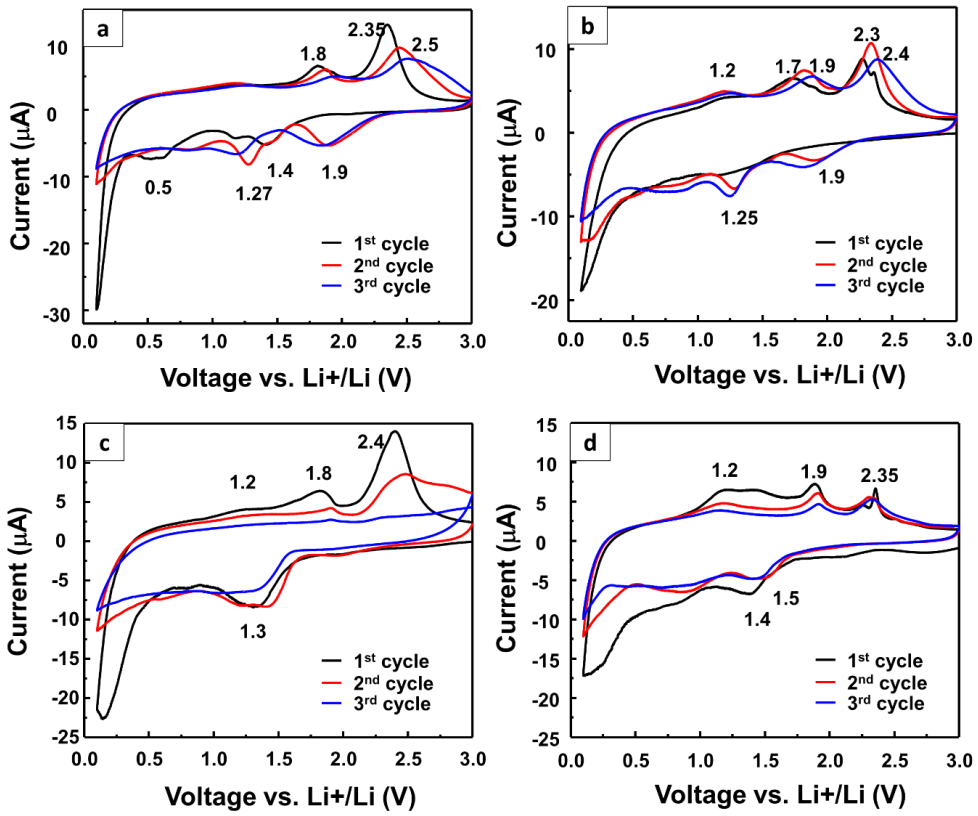

Figure 5. Cyclic voltammograms of the (**a**) as-prepared WS_2 NF, (**b**)W_2C/WS_2_2h NF, (**c**)W_2C/WS_2_4h NF, and (**d**) W_2C/WS_2_12h NF electrodes.

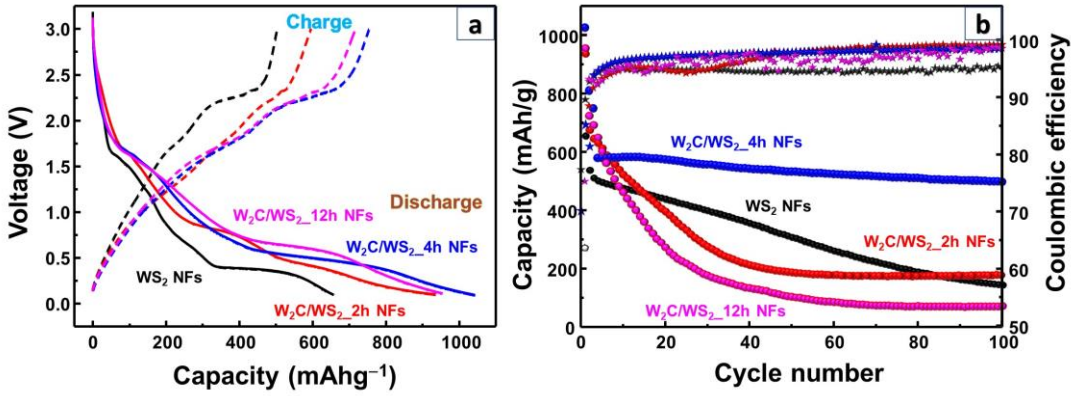

Figure 6. (**a**) Initial voltage profiles and (**b**) cyclic performance of the as-prepared WS_2 NF, W_2C/WS_2_2h NF, W_2C/WS_2_4h NF, and W_2C/WS_2_12h NF electrodes over 100 cycles.

To further investigate the performance of the NFs, their EIS measurements were carried out over the frequency range of 100 kHz–0.1 Hz at a voltage of 3.0 V. Figure 7 shows the Nyquist plots of the WS_2 and W_2C/WS_2 NF electrodes with the equivalent circuit as an inset containing the constant phase elements (CPE1, 2), series resistance (R_s), charge transfer resistance (R_{ct}), solid electrolyte resistance (R_{SEI}), and diffusion Warburg element (W). The semicircular arc corresponds to their charge transfer resistances between the interface of electrode and electrolyte [42]. The resistance values are summarized in Table 1. The WS_2 NF anode showed the highest charge transfer resistance among all the anodes investigated. The charge transfer resistance of the WS_2 NFs decreased with the addition of W_2C in the case of the W_2C/WS_2_2h and W_2C/WS_2_4h electrodes. However, it increased again for the W_2C/WS_2_12h electrode. The difference in the performance of the as-prepared W_2C/WS_2 electrodes

could be due to the different amount of W_2C in the alloys. As shown by the Raman spectrum in Figure 2b, the peak intensities of the D- and G-band from the carbon atoms in W_2C decreased when the reaction time increased, illustrating an increase in the amount of WS_2. In the case of the W_2C/WS_2_12h sample, it could have an excess amount of H_2S at 250 °C, and the applied high pressure sulfurized the weak bonding of W−C, leading to the lower amount of C, which was confirmed by Raman spectra representing the decrease of the D-band and G-band. Moreover, the flower size of the W_2C/WS_2_12h sample is about 1 μm, which is even bigger than the random size of WS_2 NFs. It should be noted that the increase in size could lead to the decrease in the conductivity [28]. When the amount and size of WS_2 increase, the resistance of the electrodes increases, as discussed in the EIS results. Specifically, the W_2C/WS_2_2h and 4h electrodes showed lower resistances compared to that of the W_2C/WS_2_12h electrode. Even though the W_2C/WS_2_2h electrode showed the lowest resistance value, the cycling performance was not stable due to the weak binding of the W_2C crystal to WS_2, leading to the gradual capacity decay, as discussed earlier. Thus, it can be concluded that the control of reaction time for the preparation of W_2C/WS_2 electrodes is crucial to optimize the overall electrochemical properties, where the $W_2C/WS_2$4h alloy is the best electrode. Computational calculations have revealed that W_2C materials are promising candidates for Li storage applications [30]. Li ions tend to adsorb on W_2C materials to form a metal cluster. Moreover, MXenes nanosheets materials exhibit high conductivity [43]. In this study, the addition of W_2C reduced the charge transfer resistance of the WS_2 NFs, and the resulting W_2C/WS_2 alloy NFs showed high storage capacity and stability for LIB applications.

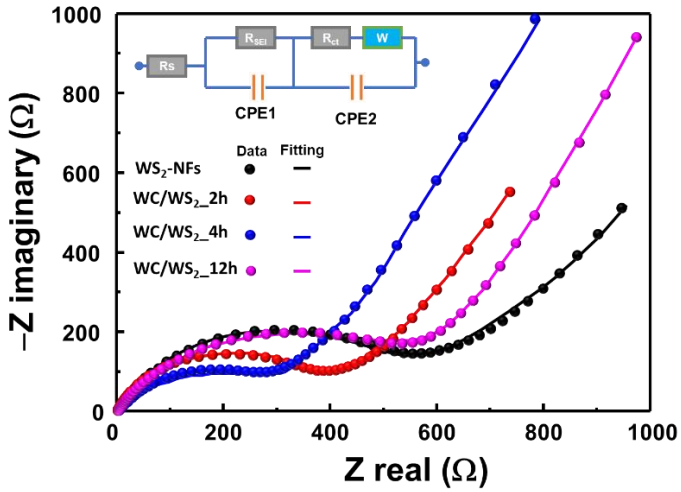

Figure 7. Nyquist plots of the as-prepared WS_2 NF, W_2C/WS_2_2h NF, W_2C/WS_2_4h NF, and W_2C/WS_2_12h NF electrodes with inset equivalent circuit.

Table 1. Comparison of resistance values extracted from equivalent circuit for the electrochemical impedance spectroscopic (EIS) measurement.

Sample	R_s	R_{ct}	R_{SEI}
WS_2 NFs	2.12	627	430
WC/WS_2_2h	3.04	381	367
WC/WS_2_4h	1.24	312	350
WC/WS_2_12h	5.41	620	422

4. Conclusions

W_2C/WS_2 NFs were successfully fabricated via a facile hydrothermal method at low temperature. The particle size of the NFs could be controlled (200 nm–1 μm). The obtained NFs exhibited high purity and well-defined hexagonal structures of W_2C and WS_2. The NF alloys were employed as anode materials for LIBs. The W_2C/WS_2_4h sample showed a high initial discharge capacity of 1040 mAh g^{-1}.

The alloy electrodes showed a low charge transfer resistance of 200–600 Ω, indicating that the W_2C/WS_2 alloy electrodes were highly conductive as compared to the WS_2 NF electrode. Among all the electrodes investigated, the W_2C/WS_2_4h electrode exhibited the highest stable capacity of up to approximately 500 mAh g^{-1} over 100 cycles, which could be attributed to the optimized W_2C in WS_2 NFs, Therefore, the W_2C/WS_2 alloy NFs prepared in this study showed a potential for energy storage and conversion applications.

Author Contributions: Conceptualization, T.P.N.; methodology, T.P.N.; validation, T.P.N.; writing—review and editing, T.P.N. and I.T.K.; visualization, T.P.N.; project administration, I.T.K.; funding acquisition, I.T.K. All authors have read and agreed to the published version of the manuscript.

Funding: This work was supported by the Korea Electric Power Corporation (grant number: R18XA02). This research was supported by the Basic Science Research Capacity Enhancement Project of Korea Basic Science Institute (National research Facilities and Equipment Center) and was funded by the Ministry of Education. (2019R1A6C1010016).

Conflicts of Interest: The authors declare no conflict of interest.

References

1. Xu, M.; Liang, T.; Shi, M.; Chen, H. Graphene-Like Two-Dimensional Materials. *Chem. Rev.* **2013**, *113*, 3766–3798. [CrossRef] [PubMed]
2. Matte, H.S.; Gomathi, A.; Manna, A.K.; Late, D.J.; Datta, R.; Pati, S.K.; Rao, C.N. MoS_2 and WS_2 analogues of graphene. *Angew. Chem. Int. Ed. Engl.* **2010**, *49*, 4059–4062. [CrossRef]
3. Kolobov, A.V.; Tominaga, J. *Two-Dimensional Transition-Metal. Dichalcogenides*; Springer International Publishing: Cham, Switzerland, 2016.
4. Kalambate, P.K.; Gadhari, N.S.; Li, X.; Rao, Z.; Navale, S.T.; Shen, Y.; Patil, V.R.; Huang, Y. Recent advances in MXene–based electrochemical sensors and biosensors. *TrAC Trends Anal. Chem.* **2019**, *120*, 115643. [CrossRef]
5. Naguib, M.; Mochalin, V.N.; Barsoum, M.W.; Gogotsi, Y. 25th Anniversary Article: MXenes: A New Family of Two-Dimensional Materials. *Adv. Mater.* **2014**, *26*, 992–1005. [CrossRef]
6. Nguyen, T.P.; Tuan Nguyen, D.M.; Tran, D.L.; Le, H.K.; Vo, D.-V.N.; Lam, S.S.; Varma, R.S.; Shokouhimehr, M.; Nguyen, C.C.; Le, Q.V. MXenes: Applications in electrocatalytic, photocatalytic hydrogen evolution reaction and CO_2 reduction. *Mol. Catal.* **2020**, *486*, 110850. [CrossRef]
7. Gatensby, R.; McEvoy, N.; Lee, K.; Hallam, T.; Berner, N.C.; Rezvani, E.; Winters, S.; O'Brien, M.; Duesberg, G.S. Controlled synthesis of transition metal dichalcogenide thin films for electronic applications. *Appl. Surf. Sci.* **2014**, *297*, 139–146. [CrossRef]
8. Phung, V.-D.; Jung, W.-S.; Kim, J.-H.; Lee, S.-W. Gold nanostructures electrodeposited on graphene oxide-modified indium tin oxide glass as a surface-enhanced Raman scattering-active substrate for ultrasensitive detection of dopamine neurotransmitter. *Jpn. J. Appl. Phys.* **2018**, *57*, 08PF02. [CrossRef]
9. Nguyen, Q.H.; Hur, J. MoS_2-C-TiC Nanocomposites as New Anode Materials for High-Performance Lithium-Ion Batteries. *J. Nanosci. Nanotechnol.* **2019**, *19*, 996–1000. [CrossRef]
10. Nguyen, Q.H.; Nguyen, Q.H.; Hur, J. High-Performance ZnTe-TiO_2-C nanocomposite with half-cell and full-cell applications as promising anode material for Li-Ion batteries. *Appl. Surf. Sci.* **2020**, *509*, 144718. [CrossRef]
11. Liu, N.; Choi, W.; Kim, H.; Jung, C.; Kim, J.; Choo, S.H.; Kwon, Y.; An, B.-S.; Hong, S.; So, S.; et al. Rapid and mass-producible synthesis of high-crystallinity $MoSe_2$ nanosheets by ampoule-loaded chemical vapor deposition. *Nanoscale* **2020**, *12*, 6991–6999. [CrossRef] [PubMed]
12. Tran, A.-V.; Shim, K.; Vo Thi, T.-T.; Kook, J.-K.; An, S.S.A.; Lee, S.-W. Targeted and controlled drug delivery by multifunctional mesoporous silica nanoparticles with internal fluorescent conjugates and external polydopamine and graphene oxide layers. *Acta Biomater.* **2018**, *74*, 397–413. [CrossRef] [PubMed]
13. Naguib, M.; Kurtoglu, M.; Presser, V.; Lu, J.; Niu, J.; Heon, M.; Hultman, L.; Gogotsi, Y.; Barsoum, M.W. Two-Dimensional Nanocrystals Produced by Exfoliation of Ti_3AlC_2. *Adv. Mater.* **2011**, *23*, 4248–4253. [CrossRef] [PubMed]
14. Mashtalir, O.; Naguib, M.; Mochalin, V.N.; Dall'Agnese, Y.; Heon, M.; Barsoum, M.W.; Gogotsi, Y. Intercalation and delamination of layered carbides and carbonitrides. *Nat. Commun.* **2013**, *4*, 1–7. [CrossRef] [PubMed]

15. Naguib, M.; Halim, J.; Lu, J.; Cook, K.M.; Hultman, L.; Gogotsi, Y.; Barsoum, M.W. New Two-Dimensional Niobium and Vanadium Carbides as Promising Materials for Li-Ion Batteries. *J. Am. Chem. Soc.* **2013**, *135*, 15966–15969. [CrossRef]
16. Tang, Q.; Zhou, Z.; Shen, P. Are MXenes Promising Anode Materials for Li Ion Batteries? Computational Studies on Electronic Properties and Li Storage Capability of Ti_3C_2 and $Ti_3C_2X_2$ (X = F, OH) Monolayer. *J. Am. Chem. Soc.* **2012**, *134*, 16909–16916. [CrossRef]
17. Wang, Y.; Li, Y.; Qiu, Z.; Wu, X.; Zhou, P.; Zhou, T.; Zhao, J.; Miao, Z.; Zhou, J.; Zhuo, S. Fe_3O_4@Ti_3C_2 MXene hybrids with ultrahigh volumetric capacity as an anode material for lithium-ion batteries. *J. Mater. Chem. A* **2018**, *6*, 11189–11197. [CrossRef]
18. Zhang, C.; Park, S.-H.; Seral-Ascaso, A.; Barwich, S.; McEvoy, N.; Boland, C.S.; Coleman, J.N.; Gogotsi, Y.; Nicolosi, V. High capacity silicon anodes enabled by MXene viscous aqueous ink. *Nat. Commun.* **2019**, *10*, 1–9. [CrossRef]
19. Nayak, A.K.; Pradhan, D. Microwave-Assisted Greener Synthesis of Defect-Rich Tungsten Oxide Nanowires with Enhanced Photocatalytic and Photoelectrochemical Performance. *J. Phys. Chem. C* **2018**, *122*, 3183–3193. [CrossRef]
20. Meyer, J.; Hamwi, S.; Kröger, M.; Kowalsky, W.; Riedl, T.; Kahn, A. Transition Metal Oxides for Organic Electronics: Energetics, Device Physics and Applications. *Adv. Mater.* **2012**, *24*, 5408–5427. [CrossRef]
21. Emin, S.; Altinkaya, C.; Semerci, A.; Okuyucu, H.; Yildiz, A.; Stefanov, P. Tungsten carbide electrocatalysts prepared from metallic tungsten nanoparticles for efficient hydrogen evolution. *Appl. Catal. B* **2018**, *236*, 147–153. [CrossRef]
22. Choi, H.; Kim, B.; Ko, M.J.; Lee, D.-K.; Kim, H.; Kim, S.H.; Kim, K. Solution processed WO_3 layer for the replacement of PEDOT:PSS layer in organic photovoltaic cells. *Org. Electron.* **2012**, *13*, 959–968. [CrossRef]
23. Li, W.-J.; Fu, Z.-W. Nanostructured WO_3 thin film as a new anode material for lithium-ion batteries. *Appl. Surf. Sci.* **2010**, *256*, 2447–2452. [CrossRef]
24. Chen, T.-Y.; Chang, Y.-H.; Hsu, C.-L.; Wei, K.-H.; Chiang, C.-Y.; Li, L.-J. Comparative study on MoS_2 and WS2 for electrocatalytic water splitting. *Int. J. Hydrogen Energy* **2013**, *38*, 12302–12309. [CrossRef]
25. Lukowski, M.A.; Daniel, A.S.; English, C.R.; Meng, F.; Forticaux, A.; Hamers, R.J.; Jin, S. Highly active hydrogen evolution catalysis from metallic WS_2 nanosheets. *Energy Environ. Sci.* **2014**, *7*, 2608–2613. [CrossRef]
26. Chen, Z.; Gong, W.; Cong, S.; Wang, Z.; Song, G.; Pan, T.; Tang, X.; Chen, J.; Lu, W.; Zhao, Z. Eutectoid-Structured WC/W_2C heterostructures: A new platform for long-term alkaline hydrogen evolution reaction at low overpotentials. *Nano Energy* **2020**, *68*, 104335. [CrossRef]
27. Feng, C.; Huang, L.; Guo, Z.; Liu, H. Synthesis of tungsten disulfide (WS_2) nanoflakes for lithium ion battery application. *Electrochem. Commun.* **2007**, *9*, 119–122. [CrossRef]
28. Srinivaas, M.; Wu, C.-Y.; Duh, J.-G.; Wu, J.M. Highly Rich 1T Metallic Phase of Few-Layered WS_2 Nanoflowers for Enhanced Storage of Lithium-Ion Batteries. *ACS Sustain. Chem. Eng.* **2019**, *7*, 10363–10370. [CrossRef]
29. Gong, Q.; Wang, Y.; Hu, Q.; Zhou, J.; Feng, R.; Duchesne, P.N.; Zhang, P.; Chen, F.; Han, N.; Li, Y.; et al. Ultrasmall and phase-pure W_2C nanoparticles for efficient electrocatalytic and photoelectrochemical hydrogen evolution. *Nat. Commun.* **2016**, *7*, 1–8. [CrossRef]
30. Zhang, Y. First principles prediction of two-dimensional tungsten carbide (W_2C) monolayer and its Li storage capability. *Comput. Condens. Matter* **2017**, *10*, 35–38. [CrossRef]
31. Nguyen, T.P.; Choi, K.S.; Kim, S.Y.; Lee, T.H.; Jang, H.W.; Van Le, Q.; Kim, I.T. Strategy for controlling the morphology and work function of W_2C/WS_2 nanoflowers. *J. Alloys Compd.* **2020**, *829*, 154582. [CrossRef]
32. Nguyen, T.P.; Kim, S.Y.; Lee, T.H.; Jang, H.W.; Le, Q.V.; Kim, I.T. Facile synthesis of W_2C@WS_2 alloy nanoflowers and their hydrogen generation performance. *Appl. Surf. Sci.* **2020**, *504*, 144389. [CrossRef]
33. Rout, C.S.; Joshi, P.D.; Kashid, R.V.; Joag, D.S.; More, M.A.; Simbeck, A.J.; Washington, M.; Nayak, S.K.; Late, D.J. Superior field emission properties of layered WS_2-RGO nanocomposites. *Sci. Rep.* **2013**, *3*, 1–8. [CrossRef] [PubMed]
34. Kurlov, A.S.; Gusev, A.I. Tungsten carbides and W-C phase diagram. *Inorg. Mater.* **2006**, *42*, 121–127. [CrossRef]
35. Litasov, K.D.; Shatskiy, A.; Fei, Y.W.; Suzuki, A.; Ohtani, E.; Funakoshi, K. Pressure-Volume-Temperature equation of state of tungsten carbide to 32 GPa and 1673 K. *J. Appl. Phys.* **2010**, *108*, 053513. [CrossRef]

36. Molina-Sánchez, A.; Wirtz, L. Phonons in single-layer and few-layer MoS_2 and WS_2. *Phys. Rev. B* **2011**, *84*, 155413. [CrossRef]
37. Yan, Y.; Xia, B.; Qi, X.; Wang, H.; Xu, R.; Wang, J.-Y.; Zhang, H.; Wang, X. Nano-Tungsten carbide decorated graphene as co-catalysts for enhanced hydrogen evolution on molybdenum disulfide. *Chem. Commun.* **2013**, *49*, 4884–4886. [CrossRef] [PubMed]
38. Cheng, Y.; Pang, K.; Wu, X.; Zhang, Z.; Xu, X.; Ren, J.; Huang, W.; Song, R. In Situ Hydrothermal Synthesis MoS_2/Guar Gum Carbon Nanoflowers as Advanced Electrocatalysts for Electrocatalytic Hydrogen Evolution. *ACS Sustain. Chem. Eng.* **2018**, *6*, 8688–8696. [CrossRef]
39. Shiva, K.; Ramakrishna Matte, H.S.S.; Rajendra, H.B.; Bhattacharyya, A.J.; Rao, C.N.R. Employing synergistic interactions between few-layer WS_2 and reduced graphene oxide to improve lithium storage, cyclability and rate capability of Li-ion batteries. *Nano Energy* **2013**, *2*, 787–793. [CrossRef]
40. Mak, K.F.; He, K.; Lee, C.; Lee, G.H.; Hone, J.; Heinz, T.F.; Shan, J. Tightly bound trions inmonolayer MoS2. *Nat. Mater.* **2013**, *12*, 207–211. [CrossRef]
41. Zhang, C.; Ma, Y.; Zhang, X.; Abdolhosseinzadeh, S.; Sheng, H.; Lan, W.; Pakdel, A.; Heier, J.; Nüesch, F. Two-Dimensional Transition Metal Carbides and Nitrides (MXenes): Synthesis, Properties, and Electrochemical Energy Storage Applications. *Energy Environ. Mater.* **2020**, *3*, 29–55. [CrossRef]
42. Moya, A.A. Identification of characteristic time constants in the initial dynamic response of electric double layer capacitors from high-frequency electrochemical impedance. *J. Power Sour.* **2018**, *397*, 124–133. [CrossRef]
43. Samad, A.; Shafique, A.; Kim, H.J.; Shin, Y.-H. Superionic and electronic conductivity in monolayer W_2C: Ab initio predictions. *J. Mater. Chem. A* **2017**, *5*, 11094–11099. [CrossRef]